Pressured-induced structural phase transition and superconductivity in $NaSn_5$

Chun-Mei Hao[1], Yunguo Li[1,2], Hong-Mei Huang[1], Yinwei Li[1] and Yan-Ling Li[1]**

1. School of Physics and Electronic Engineering, Jiangsu Normal University, Xuzhou 221116, China
2. Department of Earth Sciences, UCL, Gower Street, London, WC1E 6BT, UK

ABSTRACT: The structural and electronic properties of tin-rich compound $NaSn_5$ were investigated under pressure up to 10 GPa based on the evolutionary algorithm (EA) technique coupled with first-principles total energy calculations. Upon compression, the known metallic tetragonal *P*-42_1m phase transforms into a metallic hexagonal *P*6/*mmm* phase at 1.85 GPa accompanied by an unusual change of existing form of Sn atoms. The *P*6/*mmm* phase can be interpreted as a quasi-layered sandwich structure with two Sn layers and one sodium layer. The presence of softening phonon modes and the existence of Fermi pockets together with the obvious Fermi surface nesting indicate a strong electron-phonon coupling (EPC) and thus potential superconductivity in *P*6/*mmm* phase. The strong EPC in *P*6/*mmm* phase is mainly attributed to the phonons from Sn1 atoms together with electrons from the Sn1-p_y and Sn1-p_z states. The calculated superconducting critical temperature T_c of the *P*6/*mmm* phase is 5.91 K at 1.85 GPa. This study provides a new clue for designing intercalated compounds with superconductivity.

1. INTRODUCTION

Study on the Na-Sn system started a century ago[1], but the more concentrated study began in the 21st century. The study of phase formation and potential curves during sodium insertion has attracted many experimental and theoretical studies,[2-5] because Na compounds with group IVA elements are considered to be a power source better than the widely used lithium-ion batteries (LIBS). Na compounds with Sn, Sb, and Pb have much large gravimetric capacities among the Na anode materials.[5-8] But, both Sb and Pb are toxic. Sn, as an environment-friendly element, has come to the foreground.[9] Moreover, many carbon-related materials were reported to be superconducting, such as alkali metal graphite intercalation compounds (GICs)[10], fullerene alkali metal compounds[11]. Due to the similarity of the graphene-like boron layers in MgB_2[12], GICs draw extensive attention, in which metallic atoms intercalate between the graphene sheets. Tin also belongs to IVA group, which may have similar properties as carbon in the precursors. However, there is no report of superconductivity in Na-Sn compounds so far. It is well known that pressure is an important method for preparing new materials and adjusting properties. Whether or not Na-Sn compounds exhibit superconductivity under pressure is a significant subject.

On the other hand, the dimensionality of the tin network in Na-Sn compounds are also the focus of researches.[13-15] Depending on the atomic ratio of Na:Sn, the dimensionality of Sn atoms can undergo big changes, from the zero dimensional "isolated" Sn anions to the dimeric Sn_2 units to the tetrahedral $[Sn_4]^{4-}$ anions, to the two-dimensional Sn layers, and to the three dimensional Sn network, presenting dimensional diversity. It is similar to the polymerization forms of Si atoms observed in the K-Si system and carbon atoms in the Ca-C system.[16-18] Eighteen compounds have been reported so far.[13, 14, 19-23] Among them, *P*-42_1m-$NaSn_5$[20], *Pmmm*-$NaSn_3$[19], *C*2/*m*-$NaSn_2$[13], *P*2/*n*-Na_7Sn_{12}[14], $I4_1/acd$-NaSn[21], $P6_3/mmc$-Na_9Sn_4[22], *I*-43*d*-$Na_{15}Sn_4$[23], *Pnma*-Na_4Sn[23] have been

experimentally reported. $NaSn_5$, is of particular interest since it has the highest tin content reported so far in the experiment. The reported *P*-42_1m-$NaSn_5$ phase was also proved to be a stable phase by the calculated thermodynamic phase diagram of the Na-Sn system.[19] Although the electronic properties of *P*-42_1m-$NaSn_5$ have been reported, there have been many open questions: (i) What is the sequence of structural phase transition under pressure? (ii) Is the $NaSn_5$ a superconductor? If yes, how about the superconducting transition temperature? Here, we have systematically investigated the crystal structures of $NaSn_5$ up to 10 GPa. A novel *P*6/*mmm* phase is identified by using the evolutionary algorithm USPEX code. The *P*-42_1m phase is followed by the *P*6/*mmm* phase above 1.85 GPa. The latter exhibits superconductivity with a critical temperature of 5.91 K at 1.85 GPa.

2. COMPUTSTIONAL METHOD

The evolutionary algorithm USPEX[24, 25] in combination with the Vienna Ab initio Simulation Package (VASP) package[26] is capable of predicting the stable structures of a compound under the specific chemical composition. The structure predictions for $NaSn_5$ were performed at 0, 5 and 10 GPa with no more than 24 atoms in the unite cell. During the structure search, a plan-wave basis set cutoff of 420 eV and a coarse k-point grid were used to perform the Brillouin-zone integrations. The first generation of structures was created randomly with a population size of 120 structures. The succeeding generations were produced by 40 % variation operator heredity, 20 % lattice mutation, and 20 % permutation. Candidate structures were further optimized by using density functional theory (DFT) calculations as implemented in the VASP code. The electron-ion interaction was described using projector augmented wave (PAW) method[27], and exchange correlation potential was within the generalized gradient approximation (GGA) in Perdew-Burke-Ernzerhof form.[28] The electron configurations $2p^63s^1$ and $4d^{10}5s^25p^2$ were treated as the valences

for Na and Sn atoms, respectively. A denser Brillouin-zone sampling was chosen to ensure total energy convergence better than 1 meV per atom. Phonon spectra calculations were carried to check the dynamical stability of the candidate structures by the finite displacement method as implemented in the PHONOPY code.[29] To explore the superconducting properties, electron-phonon coupling (EPC) of the selected structure were calculated within the framework of linear-response theory through the Quantum Espresso code.[30] Optimized norm-conserving Vanderbilt pseudopotentials[31] for Na and Sn elements were chosen with a kinetic energy cut-off of 100 Ry. The dynamical matrix was computed on the basis of a 5×5×4 mesh of phonon wave vectors. To evaluate T_c, the McMillan-Allen-Dynes modified equation[32] was used with a typical Coulomb pseudopotential (μ^*)[33, 34] of 0.11.

3. RESULTS AND DISCUSSION

3.1 Structural phase transition

The evolutionary algorithm (EA) technique, which has successfully been used to predict high pressure phases of plenty of materials[17, 18, 35], was used to search for the new phases of $NaSn_5$. In addition to the reported *P*-42$_1$*m* phase, four new competitive structures with symmetries *P*6/*mmm*, *C*2/*m*, *Immm* and *Cmmm* were obtained. The calculated enthalpy difference relative to the *P*-42$_1$*m* phase under the pressure range of 0-10 GPa are shown in Figure S1. The relative enthalpies of four competitive phases (*P*6/*mmm*, *C*2/*m*, *Immm* and *Cmmm*) with respect to the *P*-42$_1$*m* phase at 0 GPa are 0.201 eV, 0.259 eV, 0.267 eV, and 0.331 eV per formula unit (f.u.), respectively. *P*6/*mmm* phase has the closest energy to the *P*-42$_1$*m* phase at ambient pressure and is rapidly stabilized as the pressure increases. The enthalpy difference curve and crystal structures are presented in Figure 1. From Figure 1, one can clearly see that the tetragonal *P*-42$_1$*m* phase transforms to the hexagonal *P6/mmm* phase at 1.85 GPa.

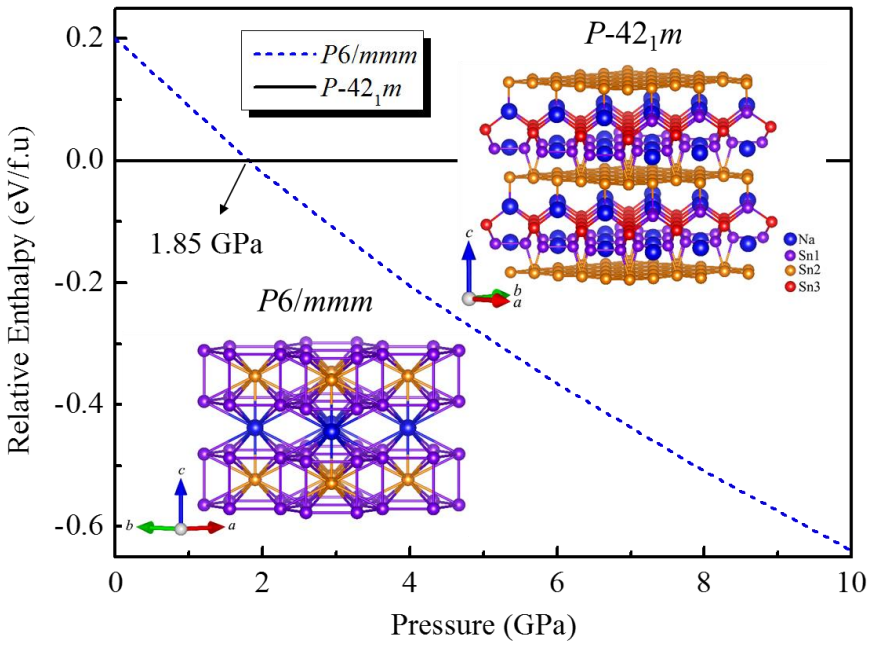

Figure 1. Relative enthalpy per chemical formula unit of *P*6/*mmm* phase with respect to the *P*-42$_1$*m* phase. The inserts show the crystal structures of two phases in which big blue balls, small purple balls, small yellow balls and small red balls represent the Na atoms, Sn1 atoms, Sn2 atom, and Sn3 atoms, respectively.

Table 1. Lattice parameters and atomic fractional coordinates of $NaSn_5$ at indicated pressures.

Space group	Pressure (GPa)	Lattice parameters (Å, deg)	Atomic Coordinate (fractional)
P-42$_1$*m*	0	$a = b = 6.3944$,	Na1 2c (0.0000, 0.5000, 0.7918)
		$c = 9.0559$	Sn1 4e (0.1578, 0.3422, 0.1819)
		$\alpha = \beta = \gamma = 90.00$	Sn2 4e (0.2491, 0.2509, 0.4957)
			Sn3 2a (0.5000, 0.5000, 0.0000)
*P*6/*mmm*	1.85	$a = b = 5.3730$,	Na1 1b (0.0000, 0.0000, 0.5000)
		$c = 6.3277$	Sn1 4h (0.6667, 0.3333, 0.7541)
		$\alpha = \beta = 90.00, \gamma = 120$	Sn2 1a (0.0000, 0.0000, 0.0000)

The calculated lattice parameters and atomic fractional coordinates of $NaSn_5$ at selected pressures are summarized in Table 1. The optimized lattice parameters for *P*-42$_1$*m* (Z=2) phase are $a = b = 6.394$ Å, and $c = 9.056$Å, which is in good agreement with the experimental values ($a = b = 6.285$Å, $c = 8.794$Å)[19] at ambient pressure. The Na atoms occupy the Wyckoff 2*c* sites and three

inequivalent Sn1, Sn2 and Sn3 atoms take the Wyckoff 4*e*, 4*e*, and 2*a*, respectively. As shown in Figure 1, the Sn1 and Sn3 atoms are four-fold coordination. The nearest-neighbor distance of Sn1-Sn1 is 2.855 Å. The next-nearest neighbors to the Sn1 are two Sn3 atom (2.9185 Å) and one Sn2 atom (2.9596 Å). The bond angles at Sn1 range from 101.544° to 117.530°. Each Sn3 atom is connected to four Sn1 atoms and forms a slightly distorted tetrahedron. The distance of Sn1-Sn3 (about 2.919 Å) is slightly higher than that (2.81 Å) in α-Sn[36], and the bond angles at Sn3 range from 108.565° to 111.30°. The Sn2 atoms that form a slightly distorted two-dimensional planar network are five-fold coordinated. The distance (about 3.198 Å) between Sn2 atoms is slightly higher than the mean interatomic distance of about 3.10 Å in *β*-tin.[36]

At 1.85 GPa, the *P*-42$_1$*m* phase with the complex three-dimensional framework formed by Sn atoms transformed into the phase *P*6/*mmm* (Z=1) in which Sn atoms form a layered structure. The *P*6/*mmm* structure can also be seen in $BaSn_5$.[37, 38, 39] In *P*6/*mmm*-$NaSn_5$, Na atoms located at the Wyckoff 1b sites. Two inequivalent Sn1 and Sn2 atoms located at the Wyckoff 4*h* and 1*a* sites. Two superimposed graphene-like layers of Sn1 atoms form a two-dimensional slab of face-sharing hexagonal prism. The nearest distance of Sn1-Sn1 is 3.102 Å within the six-membered rings of the graphene-like layers. The vertical distance between the two adjacent graphene-like layers is 3.111 Å. Sn2 atoms located in the center of the hexagonal prism have 12 nearest neighbors of Sn1 atoms. Na atoms are sandwiched by two hexagonal prisms along the z axis. Each Na atom is surrounded by twelve Sn1 atoms and two Sn2 atoms. The distance of Na-Sn varied from 3.165 to 3.494 Å at 1.85 GPa, which is shorter than the Ba-Sn distance in the *P*6/*mmm*-$BaSn_5$ (from 3.549 Å to 3.729Å). All the interatomic distances are presented in the Table 2. In other words, the phase *P*6/*mmm* can also be interpreted as a sandwich structure composed of two Sn layers and one sodium layer. The nearest distance between adjacent Sn layers is 3.218 Å. The alkali metal sodium

layer is inserted between the two Sn layers. The distances of Na-Sn1 and Na-Sn2 are 3.494 Å and 3.165 Å, respectively.

Table 2. Selected interatomic distances (Å) in *P*-42_1m phase at 0 GPa and *P*6/*mmm* phase at 1.85 GPa. The '2 ×' in the fourth row and the third column indicates that the number of Sn3 atoms at a distance of 2.9185 Å from Sn1 atoms is 2, and so on.

P-42_1m			*P*6/*mmm*		
Sn1-Sn1	2.8545	1×	Sn1-Sn1	3.1016	3×
Sn2	2.9596	1×	Sn1	3.1112	1×
Sn3	2.9185	2×	Sn2	3.4698	3×
Sn2-Sn1	2.9596	1×	Na	3.4941	3×
Sn2	3.1982	4×	Sn2-Sn1	3.4698	12×
Sn3-Sn1	2.9185	4×	Na	3.1647	2×
			Na-Sn1	3.4941	12×
			Sn2	3.1647	2×

3.2 Electronic properties

To discern the electronic structures of two phases, we calculated band structures and projected density of states (PDOS). The results show that both two phases are metals (see Figure 2(a), Figure S2 and Figure S3). For *P*-42_1m at 0 GPa, five (four valence bands and one conduction band) bands cross the Fermi level (see Figure S2). From Figure S3(a), we can clearly see a strong hybridization between Sn1 and Sn3 orbitals. The total electronic DOS at the Fermi level is approximately 1.034 states/eV per formula unit. The electronic density of states (DOS) near the Fermi level is mainly contributed by the Sn2-*p* states, while the contributions of Na, Sn1, Sn3, and Sn2-*s* states are small.

Pressure enhances the metallicity of $NaSn_5$. The total electronic DOS of *P*6/*mmm* at Fermi level is about 2.472 states/eV per formula unit at 1.85 GPa. As shown in Figure 2(a), there are five energy bands, labeled as 1, 2, 3, 4, and 5, crossing the Fermi level along the high symmetry directions in BZ. Γ point holds the D_{6h} point group. At Γ point, these five bands across the Fermi level hold three different symmetry (band 1 and band 2 hold E_{1u}, band 3 holds B_{1u}, band 4 and

band 5 hold E_{2u}). There is a two-fold degeneracy for energy bands along the H-K direction in BZ near the Fermi level. The occurrence of flat and steep slopes near the Fermi level, as a favorable condition for enhancing Cooper pair formation, has been thought to be essential for superconductivity.[10, 18] The calculated PDOS are shown in Figure S3 (b). In view of the small contribution of Sn-*d* orbital to DOS near the Fermi level, it is not shown in the Figure S3 (b). The dominant contributions to the DOS near the Fermi lever are mainly from the Sn1, especially Sn1-p_y and p_z. The orbitals from Na and Sn2 have minor contribution to DOS near the Fermi level.

Since electrons close to the Fermi level are primarily responsible for superconductivity, the Fermi surface (FS) is a key clue to understanding the electronic behavior of metals.[40] The calculated FS of *P*6/*mmm* at 1.85 GPa is shown in Figure 2(b). The labeled numbers (band 1-band 5) correspond to the labeled energy bands shown in Figure 2(a). The FS consists of 12 rounded triangular-shaped electron-like Fermi pockets around the H point (band 1), two linked electron-like flat Fermi tubes on the border of BZ (band 2), a hexagonal hollow topology hole-hole Fermi sheet (band 3), a distorted hole-like tube along the G-A direction (band 4), and three electron-hole Fermi pockets formed by two distorted sphere around A point and a gear-like sheet around the Γ point (band 5). From the Figure 2 (a), one can see that band1 and band2 mainly come from the Sn1-p_z, band 3 and band 4 mainly come from Sn1-p_x and p_y, and band5 mainly from Sn1-p_y and p_z. The hole-like bands 1 and 2 together with electron-like band 4 sheets reveal the two-dimensional behavior of *P*6/*mmm*. It can be seen that near parallel pieces of the Fermi surface exists, which favors to the EPC enhancement. Both the Fermi pockets and the obvious Fermi surface nesting indicate a strong EPC and thus potential superconductivity in *P*6/*mmm* phase.

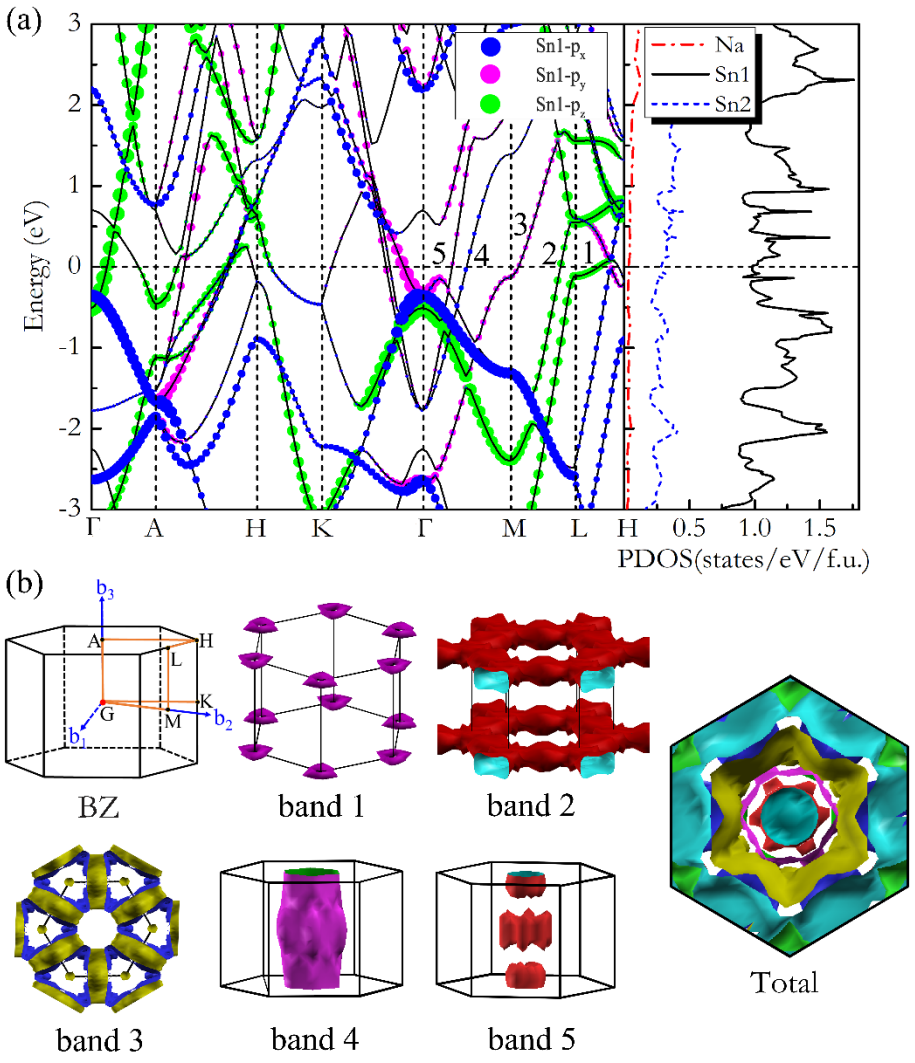

Figure 2. (a) Electronic band structure along high symmetry directions in Brillouin zone and projected density of states of *P*6/*mmm*-$NaSn_5$ (right). The sizes of the magenta, blue and green circles are proportional to the contributions from the Sn1-p_x, Sn1-p_y and Sn1-p_z orbitals, respectively. (b) Brillouin zone and Fermi surface of *P*6/*mmm*-$NaSn_5$ at 1.85 GPa. The energy bands crossing the Fermi level and the corresponding Fermi surface are labelled as 1, 2, 3, 4, and 5, respectively.

In order to further characterize the charge transfer and the bonding features, we calculated the Electron localization function (ELF) [41] of these two phases. In general, large ELF values (>0.5) correspond to the covalent bonding, lone pair or inner shell electrons, and 0.5 correspond to the

homogeneous electron gas. In order to gain further insight into the bonding nature of P6/mmm-$NaSn_5$ at 1.85 GPa, we calculated its ELF values at (1 1 0) and (0 0 1) planes as shown in Figure S4 (a) and (b), respectively. ELF values located between Sn1 and Sn1 atoms are close to 0.6. Therefore, there are localized region on the direction of the Sn1-Sn1 contact. While the ELF values located between Na and Sn are less than 0.5, which indicates no electrons localized.

3.3 Dynamic properties

To assess the dynamic stability of the $NaSn_5$ compounds, the harmonic approximation was used to calculate their phonon spectra. The phonon band structures along the high-symmetry directions in Brillouin zone (BZ) and partial atomic phonon density of states (PPHDOS) for the *P*-42_1m phase at 0 GPa and the *P*6/*mmm* phase at 1.85 GPa are shown in Figure 3 and Figure 4, respectively. The absence of imaginary frequency throughout the BZ indicates their dynamic stability. For the *P*-42_1m phase at ambient pressure, the maximum optical branch frequencies are about 203 cm^{-1} and the phonon dispersions possess a frequency gap of about 15 cm^{-1}. The flat bands along the A-M, G-Z and R-X direction may serve as an evidence of its two-dimensional feature. From PPHDOS (in the right panel of Figure 3), one can conclude that the relatively high-frequency modes (above 183 cm^{-1}) originates mostly from Na atomic vibrations. The peak centered at 153 cm^{-1} originates mainly from Sn atoms, especially from Sn3 atoms. The relatively low- and intermediate-frequencies (below 146 cm^{-1}) can be mainly attributed to Sn1 and Sn2 atoms. For the *P*6/*mmm* phase at 1.85 GPa, the maximum optical branch frequency is about 196 cm^{-1} (see Figure 4). The frequency gap is about 44 cm^{-1}, which is much higher than that in the *P*-42_1m phase. The softening

phonon modes along the A-H and G-M directions in the *P*6/*mmm* phase indicated a strong EPC effect and thus potential superconductivity.

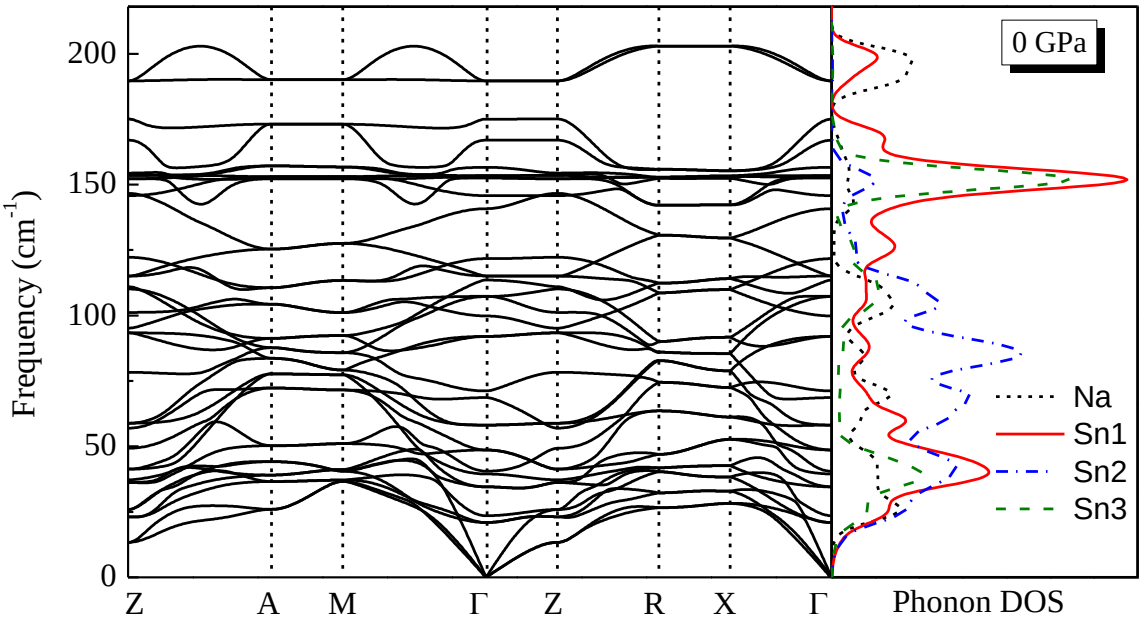

Figure 3. Phonon dispersion along the high-symmetry directions of the Brillouin zone (left panel) and the partial atomic phonon density of states (PPHDOS) (right panel) of *P*-42$_1$*m*-NaSn$_5$ at ambient pressure.

3.4 Superconducting properties

The flat and steep energy bands near the Fermi level and the soften phonon mode observed in the *P*6/*mmm* phase motivates us to explore its superconducting behavior. The calculated phonon dispersion (left panel), phonon DOS (middle panel), and Eliashberg function $\alpha^2F(\omega)$ with the integrated $\lambda(\omega)$ (right panel) for *P*6/*mmm* at 1.85 GPa are plotted in Figure 4. Na atomic vibrations dominate the spectrum range from 120 cm^{-1} to 200 cm^{-1} while Sn vibration frequencies mainly lie below 120 cm^{-1}, which agrees with the fact that the Sn atoms are much heavier than the Na atoms. The red circles in Figure 4 (left panel) represent the phonon linewidth ($\gamma_{\mathbf{q}\nu}$), and their sizes indicate

the relative contribution to the electron-phonon interaction. The vibrations between 25-120 cm^{-1} originate mostly from Sn1 atoms, contributing 75.8 % of the total λ (about 1.23). The high-frequency phonon modes above 120 cm^{-1} from the Na atoms yield only 1.3% of total λ. There are three distinct Raman modes at Γ point with calculated energies in the ranges of 62-99 cm^{-1} (E_{1g}), 102-138 cm^{-1} (A_{1g}), and 122-147 cm^{-1} (E_{2g}). A_{1g} phonon modes exhibit the largest linewidth at the Γ point indicating the large coupling with electrons. The vibrational patterns of atoms in real space for A_{1g} (ω ~111cm^{-1}) modes at the Γ point are schematically shown in Figure 4. Clearly, the Sn1 atoms vibration is out-of-plane, and Sn2 atoms and Na atoms vibration remain silent. These results indicate that strong electron-phonon coupling in the *P6/mmm* phase originates from the phonons dominates by Sn1 atoms and electrons from the Sn1-p_y and p_z states.

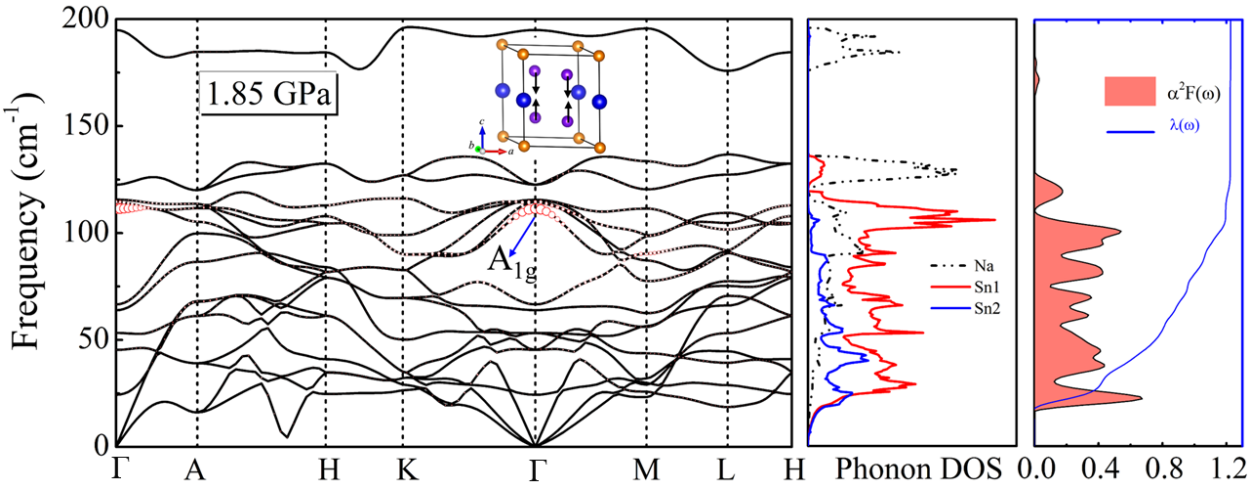

Figure 4. Phonon dispersion along the high-symmetry directions in the Brillouin zone (left panel), the partial phonon density of states (PPHDOS) (middle panel), and the Eliashberg phonon spectral function $\alpha^2F(\omega)$ and integrated EPC parameter λ as a function of frequency (right panel) of the *P6/mmm*-$NaSn_5$ at 1.85 GPa. Red circles in phonon dispersion show the EPC with the radius proportional to the respective phonon linewidth. The illustration in phonon dispersion shows A_{1g} mode at Γ point, the arrows show the direction of atomic vibration.

Electron-phonon coupling (EPC) was calculated based on Eliashberg equations.[42] The Eliashberg spectral function reads

$$\alpha^2F(\omega) = \frac{1}{2\pi N(E_f)}\sum_{\boldsymbol{q}\nu}\delta(\omega-\omega_{\boldsymbol{q}\nu})\frac{\gamma_{\boldsymbol{q}\nu}}{\hbar\omega_{\boldsymbol{q}\nu}}, \qquad (1)$$

in which $\omega_{\boldsymbol{q}\nu}$ and $\gamma_{\boldsymbol{q}\nu}$ are the frequency and linewidth for phonon mode ν at wave vector $\boldsymbol{q}$, and $N(E_f)$ is the DOS at Fermi level. The total EPC constant for the investigated compound can be determined by either the Brillouin zone summation or the frequency-space integration:

$$\lambda = \sum_{\boldsymbol{q}\nu}\lambda_{\boldsymbol{q}\nu} = 2\int\frac{\alpha^2F(\omega)}{\omega}d\omega, \qquad (2)$$

where $\lambda_{\boldsymbol{q}\nu}$ is the EPC constant for phonon mode $\mathbf{q}\nu$. The Allen-Dynes modified equation as follows

$$T_C = \frac{\omega_{\log}}{1.2}\exp\left[\frac{-1.04(1+\lambda)}{\lambda(1-0.62\mu^*)-\mu^*}\right] \qquad (3)$$

was used to evaluate the superconducting transition temperature from the value of λ determined above. The typical value 0.11 was chosen as the effective Coulomb repulsion parameter μ*. The weak metallicity of *P*-42$_1$*m* brings about a very weak electron-phonon coupling and thus very low transition temperature. For the *P*6/*mmm*-$NaSn_5$ at 1.85 GPa, the calculated EPC parameter λ is 1.23, and the estimated T_c is about 5.9 K, higher than that (4.4 K) in $BaSn_5$.[37] Moreover, the pressure dependence of T_c of *P*6/*mmm* was also given, and the values of λ, $\omega_{\log}$, and $N(E_f)$ at different pressures are listed in Table 3. It is noteworthy that as pressure increases, the calculated $\omega_{\log}$ increases, but $N(E_f)$ and λ decrease. T_c shows a monotonic decrease, from 5.91 K at 0 GPa to 4.80 K at 5 GPa and to 2.85 K at 10 GPa. Therefore, we conclude that the decrease of the T_c values under compression is mainly related to the reducing λ.

Table 3. Calculated electron-phonon coupling parameter (λ), the logarithmic average phonon frequency ω_{log}, Electronic density of states at the Fermi level $N(E_f)$ and the superconducting critical Temperature at different pressures. (The Coulomb potential μ*=0.11)

Pressure (GPa)	ω_{log} (K)	N (E_f)	λ	T_c (K)
1.85	67	19.37	1.23	5.91
5.0	80	18.16	0.96	4.80
10.0	98	16.92	0.68	2.85

Structurally, superconductors occurred in alkali and alkaline earth metal-IVA group compounds can be mainly classified into three types: monolayer structures, clathrate structures, and intercalation structures. For example, CaC_6 monolayer, the superconducting transition temperature (T_c = 1.4 K) is lower than its bulk counterpart (T_c = 11.5 K).[43] Face-centered-cubic A_3C_{60} (A = alkali metal) are common structures of the clathrate-shaped superconductors. The hydrostatic pressure on Cs_3C_{60} can change its insulating state at ambient pressure to the superconducting state at high pressure (with a maximum T_c (38 K) at ~7 GPa) without transformation.[44] Since the discovery of the first graphite intercalate superconductor, KC_8, many other GICs have been made and found to be superconducting. In order to gain further insights on the superconducting of the quasi-intercalated compound *P*6/*mmm*-$NaSn_5$, Figure 5 provides the intercalation compounds of alkali and alkaline earth metal-IVA groups alongside their superconducting critical temperatures obtained by experiment, with the exception of *P*6/*mmm*-$NaSn_5$.[45-57] All the compounds in Figure 5 are conventional superconductors based on Bardeen-Cooper-Schrieffer (BCS) theory. [58] As shown in Figure 5, superconductors with higher T_c may be designed using carbon-based compounds, in which Na, K or Ca atoms as intercalators intercalate between the carbon sheets. But overall, T_c is still relatively low due to weak electron-phonon coupling. Up to now, the highest T_c (~15 K) is from CaC_6 at high pressure of 7.5 GPa. And CaC_6

(with T_c =11.5 K) also exhibits the highest T_c at ambient pressure. $CaSi_2$ has the second-highest T_c (14 K at 15 GPa) followed by $BaSi_2$ (6.5 K at ambient pressure). *P*6/*mmm*-$NaSn_5$ ranks fifth (5.91 K at 1.85 GPa). Another question arises how can we obtain alkali metal- or alkali earth metal-IVA compounds with higher T_c. Existing studies indicate that three-dimensional (3D) framework structures are very promising candidates. This is because 3D framework structures are characterized by high crystal symmetry and large number of electrons transferred from a dopant to the host lattice. These features contribute to strong electron-phonon couplings. The idea is also well proven in the search for superconducting hydrides.[59] Although many framework structures with high T_c are metastable, but are dynamically stable at ambient pressure[60], indicating that it is very possible to synthesize 3D framework structures successfully in the experiment. The metastable compounds will probably be the candidate materials of high-temperature superconductors.

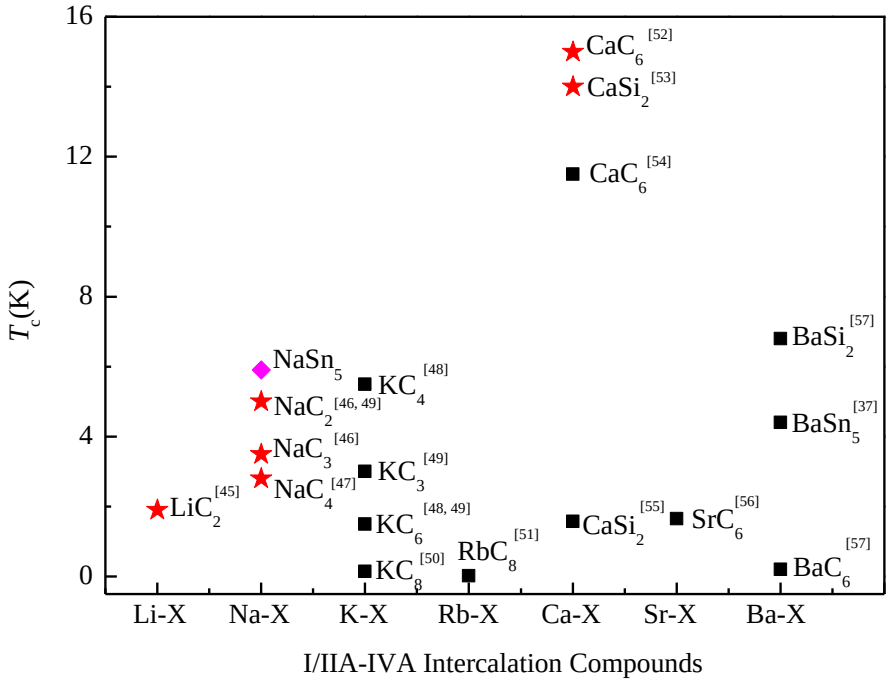

Figure 5. The superconducting critical temperature of binary intercalated compounds composed of alkali metals or alkaline earth and IVA group elements were reported in experiment. Black squares

and red pentagrams represent ambient pressure and high pressure, respectively. Magenta diamond represents $NaSn_5$ at 1.85 GPa.

4. CONCLUSION

In summary, the pressure-induced structural phase transitions and electronic properties of $NaSn_5$ have been explored up to 10 GPa based on the evolutionary algorithm crystal structural prediction method in conjunction with first-principles calculations up to 10 GPa. Our structural search reveals a new stable phase *P*6/*mmm*-$NaSn_5$ with the quasi-layered-structure feature and a lower enthalpy than the complex 3D network *P*-42_1m phase above 1.85 GPa. Both the *P*-42_1m and *P*6/*mmm* phases are dynamically stable and present metallic characteristic. Moreover, the predicted *P*6/*mmm*-$NaSn_5$ phase exhibits superconductivity with a critical temperature of about 5.9 K at the phase transition pressure. The electronic states near the Fermi level originate from the Sn1-p_y and Sn1-p_z electrons, which contribute to the strong electron-phonon coupling. The T_c decreases with the increasing pressure. Our results reveal a new type of intercalation superconductor in which group IVA element form sandwich-like layer intercalated by group IA or IIA element. This not only enriches the Na-Sn phase diagram, but also provides a new clue for designing intercalation superconductors.

AUTHOR INFORMATION

Corresponding Author

*E-mail: hmhuang@jsnu.edu.cn

ylli@jsnu.edu.cn

Notes

The authors declare no competing financial interest

ACKNOWLEDGMEN

This work is supported by the NSFC (Grant Nos. 11674131, 11981240360). We thank the use of High Performance Computing Center at JNSU.

Supporting Information Available: Enthalpy difference versus pressure curve, band structure of *P*-42_1m phase, the projected density of states, and electronic local functions of *P*6/*mmm* phase. This material is available free of charge via the Internet at http://pubs.acs.org.

REFERENCES

1. Hume-Rothery W. The System Sodium-Tin. *J. Chem. Soc.* **1928**, *131*, 947-963.
2. Ellis, L. D.; Hatchard, T. D.; Obrovac, M. N. Reversible Insertion of Sodium in Tin. *J. Electrochem. Soc.* **2012**, *159*, A1801-A1805.
3. Wang, J. W.; Liu, X. H.; Mao, S. X.; Huang, J. Y. Microstructural Evolution of Tin Nanoparticles during in Situ Sodium Insertion and Extraction. *Nano Lett*. **2012**, *12*, 5897-5902.
4. Li, Z.; Ding, J.; Mitlin, D. Tin and Tin Compounds for Sodium Ion Battery Anodes: Phase Transformations and Performance. *Acc. Chem. Res*. **2015**, *48*, 1657-1665.
5. Baggetto, L.; Bridges, C. A.; Jumas, J. C.; Mullins, D. R.; Carroll, K. J.; Meisner, R. A.; Crumlin, E. J.; Liu, X.; Yang, W.; Veith, G. M. The Local Atomic Structure and Chemical Bonding in Sodium Tin Phases. *J. Mater. Chem.* **2014**, *2*, 18959-18973.
6. Komaba, S.; Matsuura, Y.; Ishikawa, T.; Yabuuchi, N.; Murata, W.; Kuze, S. Redox Reaction of Sn-Polyacrylate Electrodes in Aprotic Na Cell. *Electrochem. Commun.* **2012**, *21*, 65-68.
7. Darwiche, A.; Marino, C.; Sougrati, M. T.; Fraisse, B.; Stievano, L.; Monconduit, L. J. Better Cycling Performances of Bulk Sb in Na-ion Batteries Compared to Li-ion Systems: An Unexpected Electrochemical Mechanism. *J. Am. Chem. Soc.* **2012**, *134*, 20805-20811.
8. Darwiche, A.; Dugas, R.; Fraisse, B.; Monconduit, L. Reinstating Lead for High-loaded Efficient Negative Electrode for Rechargeable Sodium-ion Battery. *J. Power Sources* **2016**, *304*, 1-8.
9. Zhang, B.; Rousse, G.; Foix, D.; Dugas, R.; Corte, D. A.; Tarascon, J. M. Microsized Sn as Advanced Anodes in Glyme-based Electrolyte for Na-ion Batteries. *Adv. Mater.* **2016**, *28*, 9824-9830 .
10. Li, Y. L.; Luo, W.; Chen, X. J.; Zeng, Z.; Lin, H. Q.; Ahuja, R. Formation of Nanofoam Carbon and Re-emergence of Superconductivity in Compressed CaC_6. *Sci. Rep.* **2013**, *3*, 3331.
11. Ganin, A. Y.; Takabayashi, Y.; Jeglič, P.; Arčon, D.; Potočnik, A.; Baker, P. J.; Ohishi, Y.; McDonald, M. T.; Tzirakis, M. D.; McLennan, A.; Darling, G. R.; Takata, M.; Rosseinsky, M. J.; Prassides, K. Polymorphism control of superconductivity and magnetism in Cs_3C_{60} close to the Mott transition. *Nature* **2010**, *466*, 221-225.
12. Nagamatsu, J.; Nakagawa, N.; Muranaka, T.; Zenitani, Y.; Akimitsu, J. Superconductivity at 39 K in magnesium diboride. *Nature*, **2001**, *410*, 63-64.
13. Dubois, F.; Schreyer, M,; Fässler, T. F. $NaSn_2$: A Novel Binary Zintl Phase with 2D Polyanions of Realgar-type Units $[Sn_8]^{4-}$. *Inorg. Chem.* **2005***, 44*, 477-479.
14. Fässler, T. F.; Hoffmann, S. Na_7Sn_{12}: A Binary Zintl Phase with a Two-dimensional Covalently Bonded Tin Framework. *Inorg. Chem.* **2003**, *42*, 5474-5476.

15. Fässler, T. F. Structure Motifs of Sodium Stannides on the Tin-rich Side of the Phase Diagram. Z. Anorg. *Allg. Chem.* **2006**, *632*, 1125-1129.
16. Hao, C. M.; Li, Y. G.; Huang H. M.; Li, Y. L. Structural Diversity and Electronic Properties in Potassium Silicides. *J. Chem. Phys.* **2018**, *148*, 204706.
17. Li, Y. L.; Wang, S. N.; Oganov, A. R.; Gou, H.; Smith, J. S.; Strobel, T. A. Investigation of Exotic Stable Calcium Carbides Using Theory and Experiment. *Nat. Commun.* **2015**, *6*, 6974.
18. Li, Y. L.; Luo, W.; Zeng, Z.; Lin, H. Q.; Mao, H. K.; Ahuja, R. Pressure-induced Superconductivity in CaC_2. *Proc. Natl Acad. Sci. USA* **2013**, *110*, 9289-9294.
19. Stratford, J. M.; Mayo, M.; Allan, P. K.; Pecher, O.; Borkiewicz, O. J.; Wiaderek, K. M.; Chapman, K. W.; Pickard, C. J.; Morris, A. J.; Grey, C. P. Investigating Sodium Storage Mechanisms in Tin Anodes: A Combined Pair Distribution Function Analysis, Density Functional Theory, and Solid-State NMR Approach. *J. Am. Chem. Soc.* **2017**, *139*, 7273-7286.
20. Fässler, T. F.; Kronseder, C. $NaSn_5$-eine Intermetallische Phase mit Strukturmotiven des Kovalent Aufgebauten α- und des Metallischen β-zinns. *Angew. Chem., Int. Ed.* **1998**, *110,* 1641-1644.
21. Müller, W.; Volk, K. The Crystal Structure of β-NaSn. *Z. Naturforsch. B* **1977**, *32*, 709-710.
22. Müller, W.; Volk, K. The Structures of the Phases Na_9Sn_4 and $Na_{15}Sn_4$. *Z. Naturforsch. B* **1978**, *33b*, 275-278.
23. Müller, W.; Volk, K. The Crystal Structure of $Na_{3.7}Sn$ ($\approx Na_{15}Sn_4$). *Z. Naturforsch. B* **1975**, *30*, 494-496.
24. Oganov, A. R.; Lyakhov, A. O.; Valle, M. How Evolutionary Crystal Structure Prediction Works-and Why. *Acc. Chem. Res.* **2011**, *44*, 227-237.
25. Lyakhov, A. O.; Oganov, A. R.; Stokes, H. T.; Zhu, Q. New Developments in Evolutionary Structure Prediction Algorithm USPEX. *Comput. Phys. Commun.* **2013**, *184*, 1172-1182.
26. Hafner, J.; Materials Simulations Using VASP-a Quantum Perspective to Materials Science. *Comput. Phys. Commun.* **2007**, *177*, 6-13.
27. Kresse, G.; Joubert, D. From Ultrasoft Pseudopotentials to the Projector Augmented-wave Method. *Phys. Rev. B* **1999**, *59*, 1758-1775 .
28. Perdew, J. P.; Burke, K.; Ernzerhof, M. Generalized Gradient Approximation Made Simple. *Phys. Rev. Lett.* **1996**, *77*, 3865-3868.
29. Togo, A.; Oba, F.; Tanaka, I. First-principles Calculations of the Ferroelastic Transition between Rutile-type and $CaCl_2$-type SiO_2 at High Pressures. *Phys. Rev. B* **2008**, *78*, 134106.
30. Giannozzi, P.; Baroni, S.; Bonini, N.; Calandra, M.; Car, R.; Cavazzoni, C.; Ceresoli, C.; Chiarotti, G. L.; Cococcioni, M.; Dabo, I.; Corso, A. D.; Gironcoli, S. D.; Gebauer, R.; Gerstmann, U.; Gougoussis, C.; Kokalj, A.; Lazzeri, M.; Colomer, L. M. S.; Marzari, N.; Mauri, F.; Paolini, S.; Pasquarello, A.; Paulatto, L.;

Sbraccia, C.; Scandolo, S.; Sclauzero, G.; Seitsonen A. P.; Smogunov, A.; Umari, P.; Wentzcovitch, R. M. Quantum Espresso: A Modular and Open-source Software Project for Quantum Simulations of Materials. *J. Phys: Condens. Mat.* **2009**, *21*, 395502.

31. Hamann, D. R. Optimized Norm-conserving Vanderbilt Pseudopotentials. *Phys. Rev. B* **2013**, *88*, 085117.
32. P. B., Allen; Dynes, R. C. Transition Temperature of Strong-coupled Superconductors Reanalyzed. *Phys. Rev. B* **1975**, *12*, 905-922.
33. Li, Y. L.; Stavrou, E.; Zhu, Q.; Clarke, S. M.; Li, Y.; Huang, H. M. Superconductivity in the van der Waals Layered Compound PS_2. *Phys. Rev. B*, **2019**, *99*, 220503.
34. Morel, P.; Anderson, P. W. Calculation of the superconducting state parameters with retarded electron-phonon interaction. *Physical Review* **1962**, *125*, 1263.
35. Zhang, W. W.; Oganov, A. R.; Goncharov, A. F.; Zhu, Q.; Boulfelfel, S. E.; Lyakhov, A. O.; Somayazulu, M.; Prakapenka, V. B. Unexpected Stable Stoichiometries of Sodium Chlorides. *Science* **2013**, *342*, 1502-1505.
36. Pöttgen, R. Stannides and Intermetallic Tin Compounds-Fundamentals and Applications. *Z. Kristallogr.* **2006**, *61b*, 677-698.
37. Lin, X.; Bud'ko, S. L.; Canfield, P. C. Physical Properties of Single Crystalline $BaSn_5$. Phil. Mag. **2012**, *92*, 3006-3014.
38. Fässler, T. F.; Hoffmann S.; Kronseder, C. Novel Tin Structure Motives in Superconducting $BaSn_5$-the Role of Lone Pairs in Intermetallic Compounds. *Z. Anorg. Allg. Chem.* **2001,** *627*, 2486-2492.
39. Billington, D.; Ernsting, D.; Millichamp, T. E.; Dugdale, S. B. Electron–phonon Superconductivity in $BaSn_5$. *Phil. Mag.* **2015**, *95*, 1728-1737.
40. Lebègue, S. Electronic Structure and Properties of the Fermi Surface of the Superconductor LaOFeP. *Phys. Rev. B* **2007**, *75*, 035110.
41. Becke, A. D.; Edgecombe, K. E. A Simple Measure of Electron Localization in Atomic and Molecular Systems. *J. Chem. Phys.* **1990**, *92*, 5397-5403.
42. Eliashberg, G. M. Interactions between Electrons and Lattice Vibrations in a Superconductor. *Sov. Phys. JETP* **1960**, *11*, 696-702.
43. Profeta, G.; Calandra, M.; Mauri, F. Phonon-mediated Superconductivity in Graphene by Lithium Deposition. *Nat. Phys* **2012**, *8*, 131-134.
44. Ganin, A. Y.; Takabayashi, Y.; Khimyak, Y. Z.; Margadonna, S.; Tamai, A.; Rosseinsky, M. J.; Prassides, K. Bulk Superconductivity at 38 K in a Molecular System. *Nature Mater.* **2008**, *7*, 367-371.
45. Belash, I. T.; Bronnikov, A. D.; Zharikov, O. V.; Palnichenko, A. V. Superconductivity of Graphite Intercalation Compound with Lithium C_2Li. *Solid State Commun.* **1989**, *69*, 921-923 .

46. Belash, I. T.; Bronnikov, A. D.; Zharikov, O.V.; Palnichenko, A. V. On the Superconductivity of Graphite Intercalation Compounds with Sodium. *Solid State Commun.* **1987**, *64*, 1445-1447 .
47. Smith, R. P.; Weller, T. E.; Howard, C. A.; Dean, M. P. M.; Rahnejat, K. C.; Saxena, S. S.; Ellerby, M. Superconductivity in Graphite Intercalation Compounds. *Physica C* **2015**, *514*, 50-58 .
48. Avdeev, V. V.; Zharikov, O. V.; Nalimova, V. A.; Palnichenko, A. V.; Semenenko, K. N. Superconductivity of Layered Compounds C_6K and C_4K. *Pis'ma Zh. Eksp. Teor. Fiz* **1986**, *43*, 376.
49. Belash, I. T.; Bromnikov, A. D.; Zharikov, O. V.; Palnichenko, A. V. Effect of the Metal Concentration on the Superconducting Properties of Lithium-, Sodium- and Potassium-containing Graphite Intercalation Compounds. *Synth. Met.* **1990**, *36*, 283-302.
50. Hannay, N. B.; Geballe, T. H.; Matthias, B. T.; Andres, K.; Schmidt, P.; MacNair, D. Superconductivity in Graphitic Compounds. *Phys. Rev. Lett*. **1965**, *14*, 225-226.
51. Kobayashi, M.; Enoki, T.; Inokuchi, H. Superconductivity in the First Stage Rubidium Graphite Intercalation Compound C_8Rb. *Synth. Met.* **1985**, *12*, 341-346.
52. Gauzzi, A.; Takashima, S.; Takeshita, N.; Terakura, C.; Takagi, H.; Emery, N.; Hérold, C.; Lagrange, P.; Loupias, G. Enhancement of Superconductivity and Evidence of Structural Instability in Intercalated Graphite CaC_6 under High Pressure. *Phys. Rev. Lett.* **2007**, *98*, 589-605.
53. Bordet, P.; Affronte, M.; Sanfilippo, S.; Regueiro, M. N.; Laborde, O.; Olcese, G. L.; Palenzona, A.; LeFloch, S.; Levi, D.; Hanfland, M. Structural Phase Transitions in $CaSi_2$ under High Pressure. *Phys. Rev. B* **2000**, *62*, 11392-11397.
54. Emery, N.; Hérold, C.; D'Astuto, M.; Garcia, V.; Bellin, Ch.; Marêché, J. F.; Lagrange, P.; Loupias, G. Superconductivity of Bulk CaC_6. *Phys. Rev. Lett.* **2005**, *95*, 087003.
55. McWhan, D. B.; Compton, V. B.; Silverman, M. S.; Soulen, J. R. Crystal Structure and Superconductivity of a High-pressure Phase of $CaSi_2$. *J. Less-Common Met* **1967**, *12*, 0-76.
56. Kim, J. S.; Boeri, L.; O'Brien, J. R.; Razavi, F. S.; Kremer, R. K. Superconductivity in Heavy Alkaline-earth Intercalated Graphites. *Phys. Rev. Lett.* **2007**, *99*, 027001.
57. Imai, M.; Hirota, K.; Hirano, T. Superconductivity of Trigonal $BaSi_2$. *Physica C* **1995**, *245*, 12-14.
58. Bardeen, J.; Cooper, L. N.; Schrieffer, J. R. Theory of Superconductivity. *Phys. Rev.* **1957**, *108*, 1175.
59. Peng, F.; Sun, Y.; Pickard, C. J.; Needs, R. J.; Wu Q.; Ma, Y. Hydrogen Clathrate Structures in Rare Earth Hydrides at High Pressures: Possible Route to Room-Temperature Superconductivity. *Phys. Rev. Lett.* **2017**, *119*, 107001.
60. Lu, S. Y.; Liu, H. Y.; Naumov, I. I.; Meng, S.; Li, Y. W.; Tse, J. S.; Yang, B.; Hemley, R. J. Superconductivity in dense carbon-based materials. *Phys. Rev. B* **2016**, *93,* 104509.

Table of Contents (TOC) Image

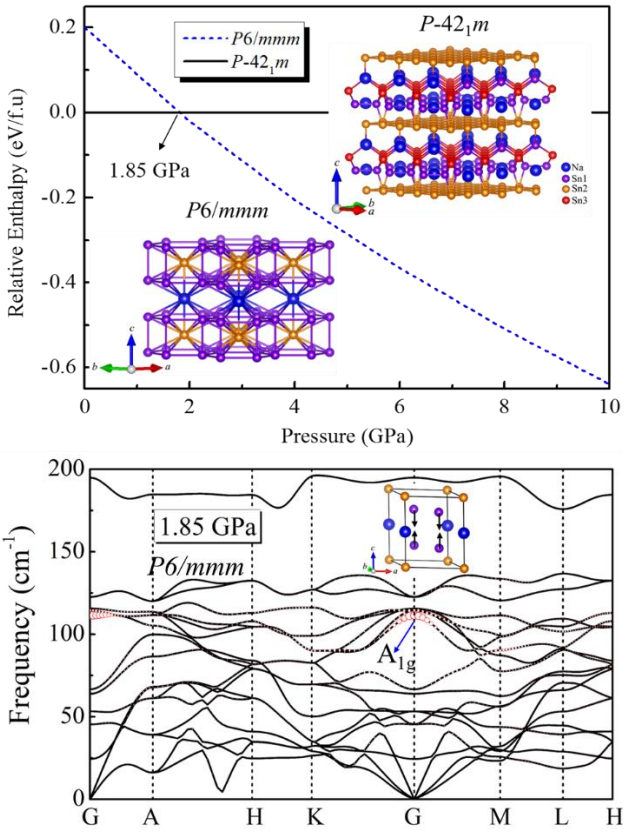

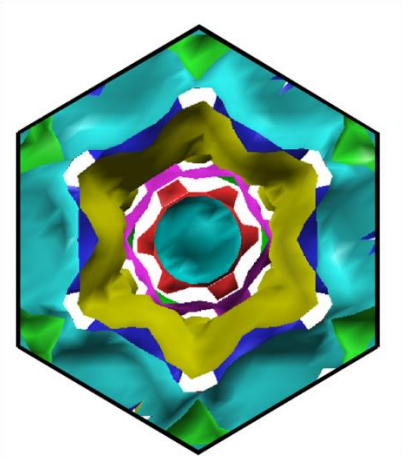

The total fermi surface of *P6/mmm*

Upon compression, the known metallic tetragonal *P*-42$_1$*m* phase transforms into a metallic quasi-layered sandwich *P6/mmm* phase at 1.85 GPa. The presence of softening phonon modes and the existence of Fermi pockets together with the obvious Fermi surface nesting indicate a strong electron-phonon coupling (EPC) in *P6/mmm*. The estimated transition temperature of metallic *P6/mmm* phase is 5.91K at 1.85 GPa.